Heating Power of Millimeter-Sized Implanted Coils for Tumor Ablation: Numerical-Analytic Analysis and Optimization

MICHAEL PRANTNER[ID][1] **AND NEJILA PARSPOUR**[ID][2]

[1]BOWA-electronic GmbH & Co. KG, 72810 Gomaringen, Germany
[2]Institute of Electrical Energy Conversion, University of Stuttgart, 70569 Stuttgart, Germany

Corresponding author: Michael Prantner (michael.prantner@bowa-medical.com)

ABSTRACT Minimally invasive thermal ablation procedures of tumors with implanted devices are very promising, especially for the repetitive treatment of deep-seated tumors. The implanted devices are heated without contact by an alternating magnetic field from outside the patient's body. In this paper, the heating power of millimeter-sized implanted coils is analyzed and optimized with a numerical-analytic analysis and the dependencies on spatial, electrical, and magnetic parameters are evaluated and presented for being able to choose the optimum implanted coil for a specific set of parameters. The analysis is done with focus on the implanted coils based on a homogeneous alternating magnetic field. A heating power of 1.5 W required for achieving an adequate rise of tissue temperature is determined in a thermal analysis and the corresponding specific absorption rate (SAR) is evaluated along with the power transfer efficiency (PTE) and the coupling coefficient for different types of implanted coils. For uncompensated implanted coils, a SAR of 306 mW/kg, a PTE of $4.62 \cdot 10^{-3}$ and a coupling coefficient of $2.49 \cdot 10^{-3}$ is achieved by a magnetic field strength of 1727 A/m, whereas a SAR of 1.84 mW/kg, a PTE of $436 \cdot 10^{-3}$ and a coupling coefficient of $2.3 \cdot 10^{-3}$ is achieved by a magnetic field strength of 134 A/m for serial compensated implanted coils. With this, the ratio of heating power to required magnetic field strength is maximized, which reduces the risk of unwanted heating of healthy tissue and other implanted devices and therefore enhances the safety as well as the well-being of the patients.

INDEX TERMS Tumors, coils, magnetic fields, hyperthermia, implants, thermal ablation, contactless, minimally invasive, power absorption, heating power.

I. INTRODUCTION

Contactless energy transfer (CET) is very advantageous in various fields of applications, such as electrical machines and dynamic charging of electric vehicles [1]–[9] and supplying energy to and monitoring of implanted medical microsystems [10]–[12]. A very important application of CET is the non invasive and the minimally invasive treatment of cancer by heating up and by ablating tumor tissue (hyperthermia). Here, tumor tissue is heated directly by eddy currents resulting from radiofrequency magnetic fields or by devices implanted or injected into the tumor and heated by an alternating magnetic field based on magnetic or ohmic losses, such as magnetic nanoparticles and permanently implanted devices [13]–[16].

Generally, hyperthermia by permanently implanted devices can be divided into two categories: Heat generation by applying electrical currents directly to the tumor tissue with electrodes [17] and heating tumor tissue indirectly by generating heat in an implanted device, which is referred to as magnetically mediated hyperthermia (MMH) [18], [19]. Since the electrical properties of human tissue change with tissue temperature and differ with tissue type, the generation of heat by electrical currents (eddy currents or currents applied directly to the tissue by an implanted device) strongly depends on tissue temperature and type of tissue. Hence, an optimization of power absorption is difficult to achieve. In contrast to that, power absorption can be optimized significantly with MMH by choosing the appropriate implant design and material properties due to power absorption is independent of tissue properties. Additionally, a more localized heating of tissue can be accomplished with MMH. The optimization of power absorption and the localization of
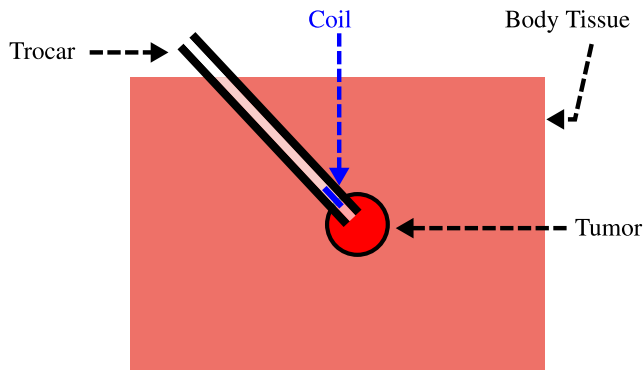
The associate editor coordinating the review of this manuscript and approving it for publication was Yiming Huo[ID].

FIGURE 1. Illustration of a minimally invasive operation technique for positioning the coils within the tumor.
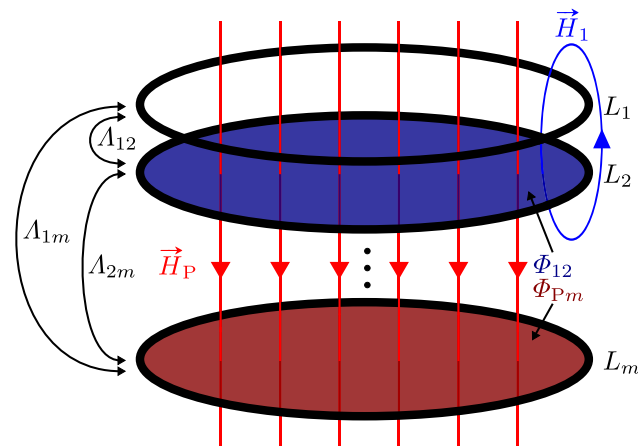

FIGURE 2. Schematic representation of m single secondary coils, which are penetrated by a magnetic field $\vec{H}_P$ created by a single or multiple primary coils. The magnetic flux Φ_{Pm}, which is received by L_m from the primary coil or coils, and the magnetic flux Φ_{12}, which is created by L_1 and received by L_2, are presented along with the magnetic conductivities Λ_{12}, Λ_{1m}, and Λ_{2m} between all single coils. Λ_{12}, Λ_{1m}, and Λ_{2m} are equal to Λ_{21}, Λ_{m1}, and Λ_{m2}, respectively.

tissue heating are essential for the well-being of the patients as unwanted heating and influencing of healthy tissue are minimized.

In the last decades, intensive research has been done on the feasibility and on heat generation with respect to a contactless thermal treatment of tumors with inductively heated implanted devices [20]–[27]. Different models for wire wound coils were presented by the authors in [28]–[33] based on numerical and analytic approaches. The frequency and the electrical conductivity for an implanted coil were analyzed and optimized in [34], whereas the radii of the primary and the secondary coils and the radii of the coil wires as well as the frequency were optimized for maximum heating efficiency in [35] for MMH. Different inductive links and coil type implants were investigated considering reactive power compensation with respect to the Q-factor [29], with respect to the maximum deliverable power under a specific absorption rate (SAR) constraint in the lower MHz range [36], and with respect to a secondary coil figure of merit comprising Q-factor, coupling coefficient and secondary coil efficiency

in the middle to upper MHz range with focus on the secondary coil [37]. A maximum power absorption with respect to an infinitely long circular cylinder is presented in [38]. In [39] and [40], an optimization of the power absorption per unit volume for ferromagnetic implanted devices heated by eddy currents is performed based on the optimum induction number by replacing a single solid ferromagnetic implant with multiple strands of wire fitting to the same cross sectional area. The authors in [41] analyzed the power absorption of a ferrite core with high permeability surrounded by a metallic sheath. The power absorption was measured and calculated based on the measured effective relative permeability of the ferrite core.

In the present paper, the heating power of wire wound and foil wound implanted coils, which corresponds to the power delivered to load (PDL), is analyzed by numerical and analytic calculations. As shown in Fig. 1, these coils are positioned within the tumor by creating a small access to the body tissue and inserting a narrow tube (trocar), through which the coils are transported to the tumor. This is referred to as minimally invasive operation technique. The resulting size restrictions with respect to the implanted coils are taken into account in the analysis done in this publication. The dependency on the diameter of the coil wire and the thickness of the foil, respectively, as well as on the electrical resistivity of the conductor material, on the frequency of the alternating magnetic field, and on the permeability of the coil core is determined and an optimization for achieving maximum heating power with respect to the spatial restrictions of a minimally invasive operation technique is done. The influence of the dimensions and of the magnetic properties of the implanted secondary coil's core on the spatial distribution of the magnetic field and the influence of the dimensions, the electrical properties and the spatial position of the coil windings on the resulting heating power are determined precisely. This has not been done in scientific literature yet. Moreover, a higher heating power per unit length is presented in this publication compared to the results reported in existing scientific literature.

The analysis in this publication focuses on achieving maximum heating power for a given alternating magnetic field. This enables to optimize the implanted coils and the field generating coils separately by assuming a very low coupling between the primary coils and the secondary implanted coil and therefore assuming a current with a constant magnitude flowing in the primary coils. Based on the numerical calculations with the finite element method (FEM), the inductance and the magnetic flux within the implanted secondary coil are evaluated precisely by determining the spatial distribution of the magnetic field influenced by the ferromagnetic core of the coil and by determining the coupling between every single winding of the implanted coil. Based on this, the heating power is calculated analytically. A thermal evaluation is done to evaluate the minimum required heating power for achieving an adequate rise of tissue temperature with respect to conduct a thermal tumor ablation. The resulting SAR, the

resulting power transfer efficiency (PTE), and the coupling coefficient are determined based on a model of the human body and based on specific primary coil configurations for the worst case scenario of deep-seated tumors, which have been analyzed by the authors in [42].

In Section II of this publication, the basics of magnetic coupling are presented, followed by the settings and the structure of the numerical-analytic analysis. In Section IV and Section V, the numerical and the analytic analyses are described in detail. Subsequently, the results of the numerical-analytic analysis are presented in Section VI along with the results of the validation, followed by a thermal analysis and the evaluation of the SAR, of the PTE, and of the coupling coefficient. Finally, the results are discussed in Section VIII and some concluding words are given in Section IX.

II. MAGNETIC COUPLING BASICS

The magnetic field created by the single windings of a secondary coil and the magnetic field created by a primary coil for CET are inhomogeneous within the ferromagnetic core of the coil. Hence, for precisely evaluating the inductance and the induced voltage of a wire wound or a foil wound coil with multiple windings and a ferromagnetic core, the coupling between every single winding and the magnetic flux created by the primary alternating magnetic field in every single winding have to be determined. In this section, the basics of magnetic coupling required for calculating the inductance, the induced voltage and the resulting current of a secondary coil for an arbitrary primary magnetic field are presented.

A. MAGNETIC CONDUCTIVITY

The inductance of a coil and the coupling between coils can be expressed in terms of the magnetic conductivity Λ, which is a measure for the influence of the material properties along the field lines of a magnetic field and for the spatial properties of a single coil or a coupled coil configuration. According to Ampère's Law

$$\oint_C \vec{H}\, d\vec{s} = \iint_A \vec{J}\, d\vec{A}, \tag{1}$$

the following equation can be derived

$$\overline{H}_s \cdot \overline{l} = N \cdot I, \tag{2}$$

where $\overline{H}_s$ denotes the average magnitude of the magnetic field strength along the average magnetic field line with the length $\overline{l}$ and I denotes the current, which is applied to a current loop with N windings [43]. Thus, the magnetic flux Φ reveals to

$$\Phi = \iint_A \vec{B}\, d\vec{A} = \overline{B}_A \cdot A$$

$$= \mu \cdot \overline{H}_s \cdot A = N \cdot I \cdot \underbrace{\frac{\mu \cdot A}{\overline{l}}}_{\Lambda}, \tag{3}$$

where A denotes the area covered by the current loop and $\overline{B}_A$ denotes the average magnetic flux density, which is perpendicular to A. Therefore, according to (3), the magnetic conductivity Λ of a single current loop ($N = 1$) can be determined with

$$\Lambda = \frac{\Phi}{N \cdot I} \tag{4}$$

by evaluating the magnetic flux Φ, which is created by applying a current I to the current loop (measurement, analytic or numerical calculation). The inductance L of a coil consisting of one or multiple windings located close to each other formed by this current loop reveals to

$$L = \frac{\Psi}{I} = \frac{N \cdot \Phi}{I} = N^2 \cdot \Lambda, \tag{5}$$

where Ψ denotes the linked magnetic flux [44].

B. SECONDARY COIL

In Fig 2, a schematic representation of m single secondary coils and of the corresponding magnetic conductivities between the coils is shown along with the exemplary magnetic fluxes Φ_{Pm} and Φ_{12}. Φ_{Pm} denotes the magnetic flux, which is created by the primary coil or coils and which is received by L_m, and Φ_{12} denotes the magnetic flux, which is created by L_1 and which is received by L_2.

The overall magnetic flux $\underline{\Phi}_k$ of the kth single coil is determined by summing up all single magnetic fluxes $\underline{\Phi}_{nk}$ generated by all coils and received by the kth coil. $\underline{\Phi}_k$ results in

$$\underline{\Phi}_k = \sum_{n=1}^{m} \underline{\Phi}_{nk} + \underline{\Phi}_{Pk}, \quad (1 \le n, k \le m; \ n, k, m \in \mathbb{N})$$

$$= \sum_{n=1}^{m} N_n \cdot \underline{I}_n \cdot \Lambda_{nk} + \underline{\Phi}_{Pk}, \tag{6}$$

where $m = N_S$ denotes the total number of secondary single coils, N_n denotes the number of windings of each single secondary coil, and I_n denotes the current in each single secondary coil. With $N_1 = N_2 = \cdots = N_m = N_{sc}$ (all single coils have N_{sc} windings) and $\underline{I}_1 = \underline{I}_2 = \cdots = \underline{I}_m = \underline{I}_S$ (the same current $\underline{I}_S$ flows in all single coils), the voltage of each single secondary coil reveals to

$$\underline{U}_k = N_{sc} \cdot \frac{d\underline{\Phi}_k}{dt} = j\omega \cdot N_{sc}^2 \cdot \underline{I}_S \cdot \sum_{n=1}^{N_S} \Lambda_{nk} + j\omega \cdot N_{sc} \cdot \underline{\Phi}_{Pk}, \tag{7}$$

where ω denotes the angular frequency of the primary magnetic field [44]. In case all single secondary coils are connected in series to form a combined secondary coil, the voltage $\underline{U}_S$ of this combined secondary coil
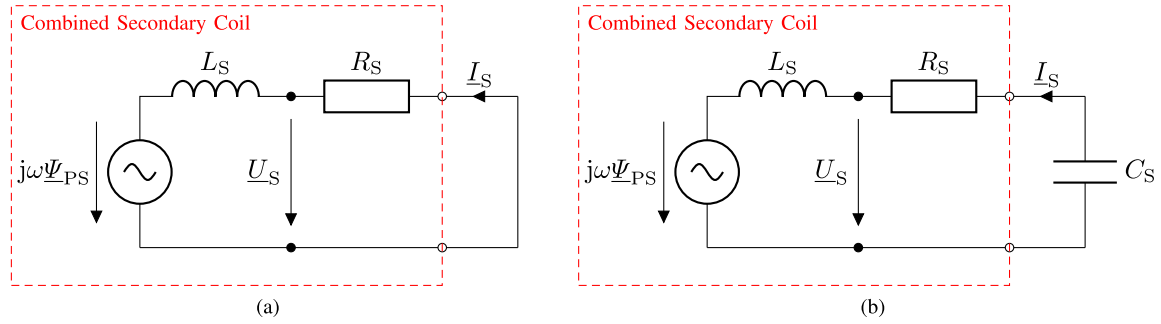
FIGURE 3. Electrical equivalent circuit of the combined secondary coil. (a) Uncompensated, (b) serial compensated with compensating capacitor C_S.

results in

$$\underline{U}_S = \sum_{k=1}^{N_S} \underline{U}_k$$

$$= j\omega \cdot \underline{I}_S \cdot N_{sc}^2 \cdot \overbrace{\underbrace{\sum_{k=1}^{N_S}\sum_{n=1}^{N_S} \Lambda_{nk}}_{N_S^2 \cdot \Lambda_S}}^{L_S} + j\omega \cdot N_{sc} \cdot \underbrace{\sum_{k=1}^{N_S} \underline{\Phi}_{Pk}}_{N_{sc} \cdot N_S \cdot \underline{\Phi}_{PS} = \underline{\Psi}_{PS}} . \quad (8)$$

Thus, the voltage $\underline{U}_S$, which is created by the alternating magnetic field in the combined secondary coil with the inductance L_S, reveals to

$$\underline{U}_S = j\omega \cdot \underline{I}_S \cdot L_S + j\omega \cdot \underline{\Psi}_{PS}. \quad (9)$$

In case a current with a constant magnitude is supplied to the primary coils or the coupling between the primary and the combined secondary coil is very low, $\underline{\Psi}_{PS}$ does not depend on the current $\underline{I}_S$ in the combined secondary coil. This is discussed in detail in Section III-C.

With

$$\underline{I}_S = -\frac{\underline{U}_S}{R_S}, \quad (10)$$

where R_S denotes the resistor, which is connected to the combined secondary coil and which generates heat, this leads to the electrical equivalent circuit of the combined secondary coil shown in Fig. 3a for the settings of the analysis carried out in this paper. These settings are introduced in Section III. In this publication, R_S is assumed to be the resistance of the coil conductor and therefore belongs to the combined secondary coil (see Section III).

III. ANALYSIS SETTINGS

The amount of energy, which causes a rise of temperature in the implanted secondary coil, depends on various parameters, such as the magnetic field strength and the spatial, magnetic and electrical properties of the implanted coil as well as on the type of reactive power compensation. This section presents the settings of the analysis, how the different parameters are taken into account, and how the results are evaluated efficiently.
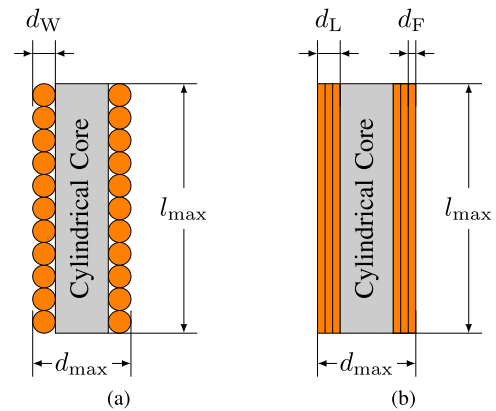

FIGURE 4. Cross section of all coil types, which are analyzed in this publication. The cylindrical core is shown in gray, whereas the conductors (coil windings of wire and coil windings of foil) are shown in orange. (a) Wire wound coil (WWC) and (b) foil wound coil (FWC).

A. DIMENSIONS

For implanting the secondary coil into the tumor, a minimally invasive operation technique is used in the contactless thermal tumor ablation procedure on which this paper is based on. Hence, the diameter of the implanted coil must not exceed the dimension of the trocar. Additionally, the length of the coil is restricted for not getting stuck in bent trocars. According to that, a maximum coil diameter of $d_{max} = 1.5$ mm and a maximum coil length of $l_{max} = 20$ mm is assumed. Therefore, the diameter of the coil core has to be decreased when increasing the diameter of the coil conductor and vice versa as the overall dimensions of the implanted coil has to be at maximum for maximizing $\underline{\Psi}_{PS}$. Increasing the diameter of the implanted coil increases $\underline{\Psi}_{PS}$ due to an increased cross sectional area and, for a coil core with a relative permeability of $\mu_r > 1$, to an increased magnetic flux density. Furthermore, increasing the length of the implanted coil increases the magnetic flux density for a coil core with a relative permeability of $\mu_r > 1$ as well. Additionally, depending on the type of conductor, more windings can be added to the coil.

B. COIL TYPES

Two different types of cylindrical implanted coils are analyzed in this work. All coil types comprise a cylindrical core

consisting of a material which has a relative permeability of $\mu_r \geq 300$ and which is electrically non-conductive. The relative permeability of the core is assumed to be independent of frequency and magnitude of the alternating magnetic field. The conductor is assumed to have a relative permeability of $\mu_r = 1$ (e.g. copper) and the electrical resistivity ρ_c. These coil types are selected for the analysis as the dimensions of the coils can be adapted to use the maximum space provided by the minimally invasive operation technique based on the cylindrical coil shape.

The resistor R_S shown in the electrical equivalent circuit (see Fig. 3), which heats up the implanted coil, is assumed to be the resulting resistance of the coil conductor. This leads to an uniform rise of temperature along the implanted coil instead of single hot spots, which increases the volume of heated tumor tissue and is advantageous for a uniform heat distribution inside the tumor. Thus, R_S depends on the conductor material, on the number of windings, and on the cross sectional area of the conductor. Additionally, the frequency of the alternating magnetic field influences R_S.

The following coil types are analyzed in this work:

- Wire wound coil (WWC): The conductor of this coil type is a wire with the diameter d_W, which is wound around the cylindrical core. The number of windings depends on the diameter of the wire. Hence, a decreased diameter of the wire leads to an increased number of windings and therefore to an increased magnetic flux $\underline{\Psi}_{PS}$, which is received from the primary coils, and an increased conductor resistance. For the WWC, solely wire diameters, which result in an integer number of windings, are taken into account. A schematic representation of the WWC is shown in Fig. 4a.
- Foil wound coil (FWC): A conductive foil with a thickness d_F is wound around the cylindrical core. The overall thickness of all windings is referred to as the thickness of the conductive layer d_L. In contrast to the WWC, the number of windings and the diameter of the core can be chosen independently by adjusting d_F. Furthermore, the coupling between the single windings is expected to be higher than between the single windings of a WWC, which leads to an increased inductance for the same number of windings. A schematic representation of the FWC is shown in Fig. 4b.

For simplifying the analysis, the single windings of the WWC are taken into account by single current loops connected in series instead of considering a helix. Additionally, the conductors are assumed to have a insulation layer on the outside boundaries to realize the insulation between the single windings. As this layer usually is very thin, it is not taken into account in the dimensions of the numerical and analytic model of the coils. Additionally, the parasitic capacitance of the secondary coils is neglected due to a low maximum frequency of the primary alternating magnetic field.

C. PRIMARY SIDE ALTERNATING MAGNETIC FIELD

Deep-seated tumors are the worst case scenario and therefore the most challenging situation for a contactless transfer of heating energy to the tumors as the energy has to be transferred over a certain distance (more than 25 cm in case a body diameter of 50 cm is assumed) from outside of the patient to the implanted device in the tumor. Hence, the primary coils for generating the alternating magnetic field have to be considerably large (approximately 50 cm in diameter, depending on primary coil system) compared to the implanted secondary coil inside the tumor (1.5 mm in diameter) due to the maximum diameter of the implanted secondary coil is limited by the minimally invasive operation technique used for positioning the secondary coil in the tumor. According to this, the coupling between the primary coils and the secondary coil is extremely low.

In the implanted secondary coil, heat is generated by an alternating magnetic field. This magnetic field is generated by one or multiple primary coils, which are located in a certain distance to the implanted secondary coil. Due to this analysis is based on the worst case scenario of deep-seated tumors, the distance between the implanted secondary coil and the primary coils is assumed to be large compared to the dimensions of the secondary coil. Therefore, the magnetic field in the surrounding area of the secondary coil is assumed to be homogeneous. Furthermore, only the component of the magnetic field parallel to the axis of the implanted coil is taken into account as this component solely contributes to heat generation. The contribution to heat generation of the remaining components, which consequently are perpendicular to the secondary coil axis, can be neglected as these components do not contribute to voltage induction in the secondary coil and no eddy currents are created in the coil core due to the core is assumed to be electrically non-conductive. Additionally, all values for the magnetic field strength are considered to be peak values.

Generally, the current $\underline{I}_P$ in the primary coil (in case of a single primary coil) can be expressed as

$$\underline{I}_P = \frac{\underline{U}_P}{j\omega \cdot N_P^2 \cdot \Lambda_P} - \frac{N_{sc} \cdot N_S \cdot \underline{I}_S \cdot \Lambda_{PS}}{N_P \cdot \Lambda_P}, \quad (11)$$

where $\underline{U}_P$ denotes the voltage supplied to the primary coil, Λ_P denotes the magnetic conductivity of the primary coil and N_P denotes the number of windings of the primary coil. The magnetic conductivity between primary and secondary coil is described by Λ_{PS}. The magnetic flux $\underline{\Psi}_{PS}$, which is created by the primary coil and received by the implanted secondary coil, can be expressed as

$$\underline{\Psi}_{PS} = N_{sc} \cdot N_S \cdot N_P \cdot \Lambda_{PS} \cdot \underline{I}_P$$

$$= \frac{N_{sc} \cdot N_S \cdot \underline{U}_P \cdot \Lambda_{PS}}{j\omega \cdot N_P \cdot \Lambda_P} - \frac{N_{sc}^2 \cdot N_S^2 \cdot \underline{I}_S \cdot \Lambda_{PS}^2}{\Lambda_P}, \quad (12)$$

The voltage of the secondary coil can generally be expressed as

$$\underline{U}_S = j\omega \cdot \underline{I}_S \cdot N_{sc}^2 \cdot N_S^2 \cdot \left(\Lambda_S - \frac{\Lambda_{PS}^2}{\Lambda_P} \right)$$
$$+ \underbrace{\frac{N_{sc} \cdot N_S \cdot \underline{U}_P \cdot \Lambda_{PS}}{N_P \cdot \Lambda_P}}_{j\omega \cdot \underline{\Psi}_{PS} \text{ for } \frac{\Lambda_{PS}^2}{\Lambda_P} \to 0 \text{ H}} . \qquad (13)$$

Thus, due to $\Lambda_{PS} \ll \Lambda_P$ and $\Lambda_{PS} \ll 1$ H for the spatial and magnetic properties, on which this analysis is based on, the magnitude of the primary current $\underline{I}_P$ and the magnitude of the magnetic flux $\underline{\Psi}_{PS}$ are considered to be independent of the current $\underline{I}_S$ in the secondary coil. Hence, according to (11) and (12), a current source with a constant magnitude is assumed to be used in this publication for supplying energy to the primary coils. With respect to maximizing the heating power, this represents the worst case scenario as the heating power increases in case of a higher coupling is assumed. Furthermore, due to $\Lambda_{PS} \ll \Lambda_P$, $\Lambda_{PS} \ll 1$ H, and $\Lambda_S \ll \Lambda_P$ and according to (13), the influence of the properties of the primary coils on the voltage $\underline{U}_S$ of the secondary coil as well as the influence of the current $\underline{I}_S$ on the current in the primary coils can be neglected. Therefore, the number, the type and the construction of the primary coils has not to be taken into account for the analysis carried out in this paper. The evaluation of the heating power $P_{S,H}$ can be done based on a given spatial distribution of the magnetic field in the area surrounding the tumor. Thus, the analysis carried out in this paper is valid for any primary coil or coil configuration supplied by an alternating current source with a constant magnitude. For $\frac{\Lambda_{PS}^2}{\Lambda_P} \to 0$ H, (13) results in (9).

D. REACTIVE POWER COMPENSATION

For increasing the heating power in the secondary coil, the reactive power in the secondary coil has to be compensated. Two basic compensating strategies are commonly used for this, the serial compensation and the parallel compensation, in which a compensating capacitor C_S is connected in series to the heating resistor R_S or in parallel to the heating resistor R_S. As the heating resistor in this analysis is represented by the conductor resistance of the secondary coil, solely a serial reactive power compensation can be realized. The electrical equivalent circuit of the secondary coil with serial reactive power compensation is shown in Fig. 3b. According to this, the analysis in this publication is done for uncompensated (UC) secondary coils and for secondary coils with serial reactive power compensation (SC).

E. STRUCTURE OF THE ANALYSIS

The analysis carried out in this work is based on a combination of numerical and analytic calculations. By a numerical calculation with FEM, the influence of the secondary coil core on a homogeneous magnetic field, which represents the magnetic field created by the primary coils, and on
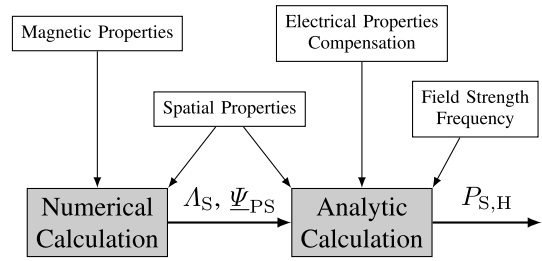

FIGURE 5. Structure of the numerical-analytic analysis carried out in this paper. The single steps of the analysis are shown (gray blocks) along with the corresponding input values (white blocks) and output values (displayed on the arrows).

the magnetic fields created by the single coil windings is determined. The spatial properties as well as the magnetic properties of the implanted coil are taken into account in the numerical calculation. Based on the resulting magnetic fields, the magnetic conductivity Λ_S of the implanted coil and the magnetic flux $\underline{\Psi}_{PS}$, which is created by the primary coils and received by the implanted secondary coil, are evaluated. The numerical calculation is described in detail in Section IV. Subsequently, with Λ_S and $\underline{\Psi}_{PS}$, the power $P_{S,H}$, which heats the secondary coil, is evaluated analytically with respect to the spatial and electrical properties of the implanted coil as well as by taking into account the magnetic field strength and the frequency of the primary magnetic field and the type of reactive power compensation. The analytic calculation is described in detail in Section V. The structure of the analysis is presented in Fig. 5. Gray blocks represent the calculations and white blocks represent the input data for these calculations. The output of the single calculation steps is shown on the arrows, which indicate the flow of data.

The structure of this analysis enables a fast and efficient evaluation of the heating ability of an implanted coil. As the influence of a cylindrical core with a relative permeability of $\mu_r > 1$ on the spatial distribution of the magnetic field can only be expressed as a function of elliptic integrals, which generally cannot be expressed in terms of elementary functions, this is done by a FEM simulation, which is, especially for a high number of coil windings, time consuming due to the magnetic field has to be evaluated at various coordinates for calculating Λ_S and $\underline{\Psi}_{PS}$. Generally, the entire analysis could be done solely by a FEM simulation, which would create high computational costs due to different electrical parameters have to be taken into account and due to the FEM simulation has to be recalculated for every single value for all electrical parameters. By considering the electrical parameters and the type of reactive power compensation in an analytic way based on the results of the FEM simulation, the flexibility of the entire analysis is enhanced and the duration is reduced.

IV. NUMERICAL ANALYSIS

The numerical calculations are controlled by MATLAB and are done with COMSOL based on a FEM model by using the LiveLink interface of COMSOL and MATLAB. For reducing computational costs without loosing accuracy, it is taken
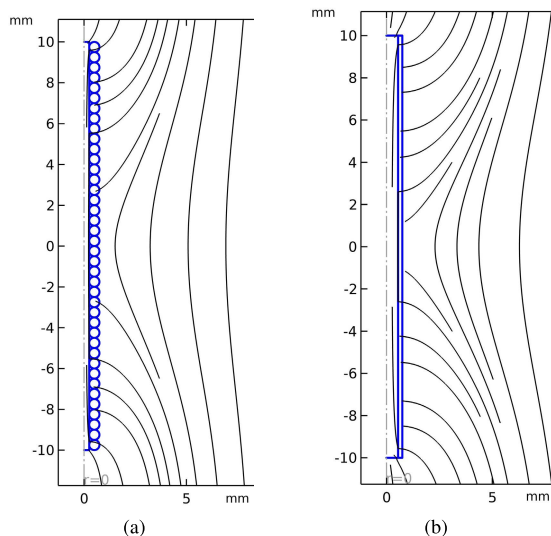
FIGURE 6. Two-dimensional FEM models of the secondary coils in the *rz*-plane at $\varphi = 0$ with the magnetic field lines originating from a homogeneous primary magnetic field for a relative permeability of the coil core of $\mu_r = 2100$. The dashed and dotted lines represent the middle axes of the coils and the symmetry axes of the FEM models. (a) WWC with $d_W = 0.5$ mm, (b) FWC with a single winding and $d_L = 0.2$ mm.

TABLE 1. Parameter sets.

Parameter	Min.	Max.
Diameter of Wire (mm)	0.02	0.69
Number of Windings WWC	29	1000
Thickness of Layer (mm)	0.02	0.69
Number of Windings FWC	1	10
Diameter of Core (mm)	0.1	1.46
Relative Permeability of Core	300	2100
Electrical Resistivity ($\mu\Omega \cdot$ m)	0.016 [a]	3
Frequency (kHz)	10	100

[a] Electrical resistivity of silver

advantage of the rotational symmetry of the coil types in the FEM model. Therefore, solely the values in the *rz*-plane at $\varphi = 0$ are calculated and rotated around the middle axis of the core for evaluating Λ_S and $\underline{\Psi}_{PS}$. The FEM models of a WWC and a FWC are shown in Fig. 6 along with the magnetic field lines originating from a homogeneous primary magnetic field. In the numerical analysis, parameter sets for the coil wire diameter d_W (WWC), for the thickness of layer d_L (FWC), for the number of windings N_S (FWC, N_S for WWC results from d_W), and for the relative permeability μ_r of the core (WWC and FWC) are calculated. The results of the numerical analysis are summarized and presented in Fig. 7 and an overview on the parameter sets used in the numerical and the analytic analysis is given in Table 1.

A. MAGNETIC CONDUCTIVITY OF THE SECONDARY COIL
Due to the magnetic conductivity between two coils or two windings does not depend on direction (e.g. $\Lambda_{12} = \Lambda_{21}$), only half of all winding combinations have to be calculated, according to

$$\Lambda_S = \frac{1}{N_S^2} \cdot \sum_{k=1}^{N_S} \sum_{n=1}^{N_S} \Lambda_{nk} = \frac{2}{N_S^2} \cdot \sum_{k=1}^{N_S} \sum_{n=k}^{N_S} \Lambda_{nk}, \quad (14)$$

which is derived from (8).

The coupling and hence the magnetic conductivity Λ_{nk} between the single windings is different for every combination of two windings. Every single winding therefore contributes differently to the combined magnetic conductivity Λ_S of the secondary coil. Λ_{nk} depends on the position relative to the core and the distance between the windings, on the diameter of the winding as well as on the relative permeability μ_r of the core.

For calculating Λ_{nk} for all winding pairs, a current I_{FEM} is applied successively to every winding and the resulting magnetic flux Φ_{nk}, which is received from the other windings and the source winding itself, is evaluated. In this evaluation step, the winding, to which the current is applied to, is the only source of a magnetic field. No magnetic field is generated by the primary coils in this step. According to (4), Λ_{nk} is calculated with

$$\Lambda_{nk} = \frac{\Phi_{nk}}{N \cdot I_{FEM}} \quad (15)$$

and $N = 1$. Subsequently, Λ_S is calculated with (14).

B. RECEIVED MAGNETIC FLUX FROM PRIMARY COILS
As described in Section III-C, a homogeneous alternating magnetic field parallel to the axis of the core is assumed to be created by the primary coils in the area surrounding the tumor. This magnetic field is implemented as boundary condition on the outside boundaries of the FEM model with a magnitude of $H_{FEM} = 1 \frac{A}{m}$. Furthermore, no current is applied to any winding of the secondary coil in this evaluation step. Due to $\underline{\Psi}_{PS} \propto \underline{H}_{FEM}$, $\underline{\Psi}_{PS}$ can be calculated analytically for any magnitude of the magnetic field with the result of this numerical calculation.

The magnetic flux $\underline{\Phi}_{Pk}$, which is received from the primary coils, is different for every single winding of the implanted secondary coil and depends on the position of the winding relative to the core, on the diameter of the windings, and on the relative permeability of the core as well as on the local magnitude of the magnetic flux density. $\underline{\Phi}_{Pk}$ is determined for every single winding and subsequently the linked magnetic flux $\underline{\Psi}_{PS}$ is evaluated according to (8) with

$$\underline{\Psi}_{PS} = N_{sc} \cdot \sum_{k=1}^{N_S} \underline{\Phi}_{Pk}. \quad (16)$$

As a single winding represents a coil with one winding, N_{sc} results in 1 for the analysis carried out in this paper.

V. ANALYTIC ANALYSIS
Based on the results of the numerical analysis, the heating power $P_{S,H}$, which is generated in the secondary coil, is evaluated analytically with MATLAB. In contrast to the numerical analysis, the electrical properties of the secondary coil and the type of reactive power compensation are taken into consideration, whereas the same parameter sets for the spatial parameters are used for both analyses. Additionally, the magnitude of the magnetic field strength and the frequency of the primary alternating magnetic field are taken into account analytically.
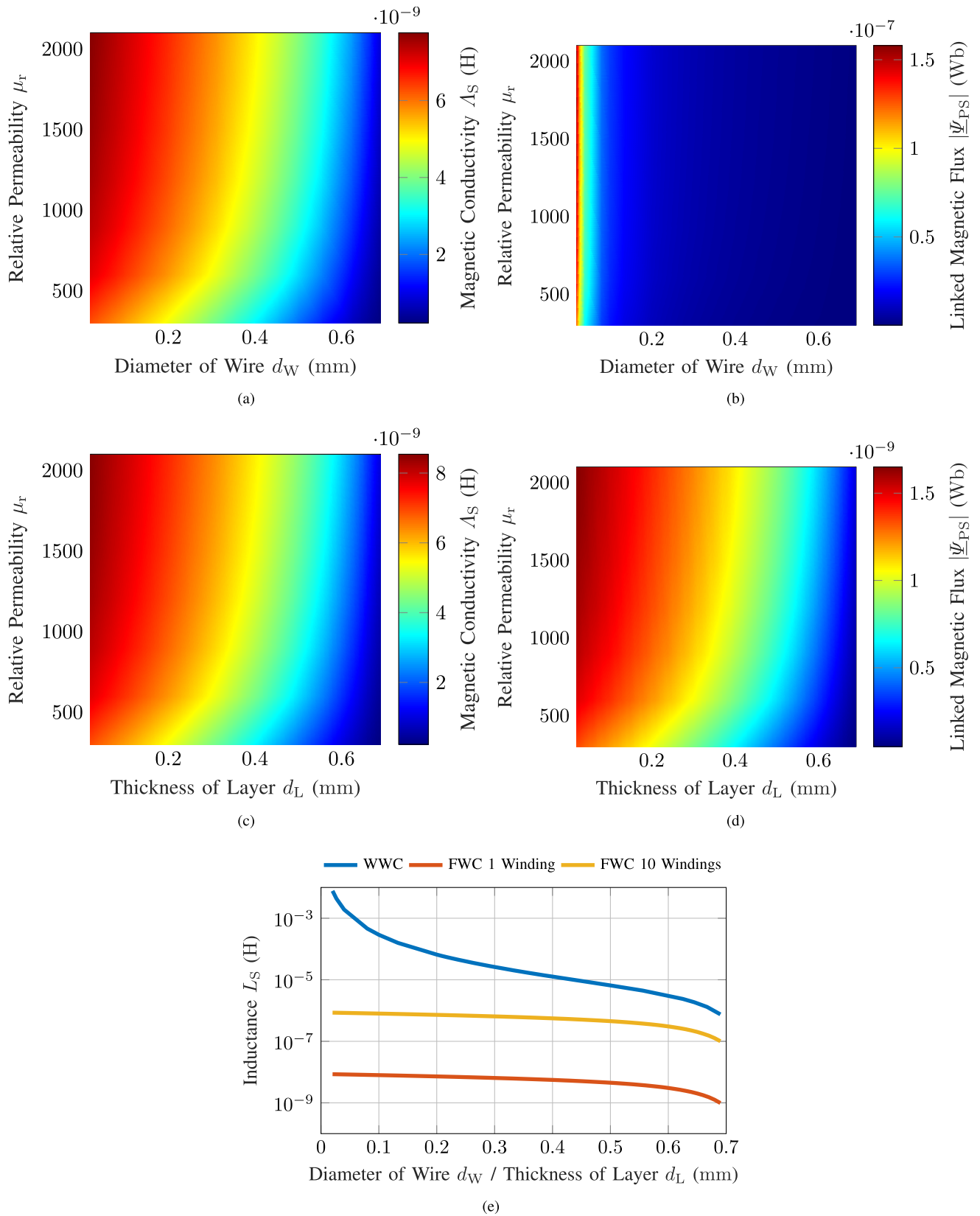
FIGURE 7. Results of the numerical evaluation for the diameter of the wire d_W (WWC), for the thickness of the conductor layer d_L (FWC), and for the relative permeability μ_r of the core. (a) Magnetic conductivity Λ_S and (b) magnitude of the linked magnetic flux $\underline{\Psi}_{PS}$ for WWC, (c) magnetic conductivity Λ_S and (d) magnitude of the linked magnetic flux $\underline{\Psi}_{PS}$ for FWC with 10 windings, (e) inductance L_S of WWC, FWC with a single winding, and FWC with 10 windings for $\mu_r = 2100$.
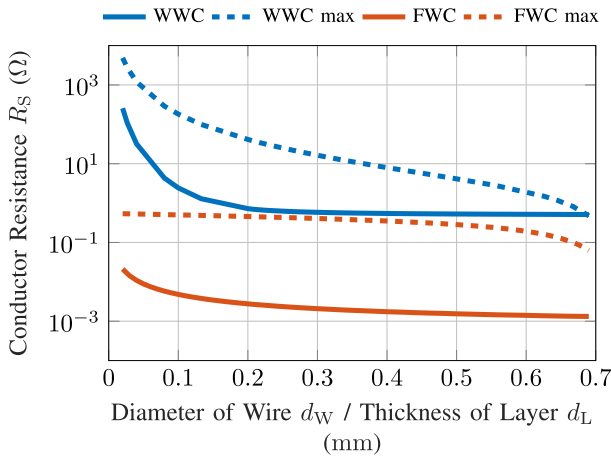
FIGURE 8. Conductor resistance R_S including the resistance of the short circuit connection from the first to the last winding of the coils and the resistance, for which the maximum heating power is achieved, of WWC and FWC with 10 windings for the diameter of the wire (WWC) and for the thickness of the conductor layer (FWC). $f = 100$ kHz and $\rho_c = 17.25$ n$\Omega \cdot$ m are assumed to represent the electrical resistivity of copper according to [45].

By applying different input values for Λ_S and $\underline{\Psi}_{PS}$ and by applying different equations for determining the conductor resistance R_S of the secondary coil, the same analytic model can be used for WWC and FWC.

A. SECONDARY CONDUCTOR RESISTANCE

The conductor resistance of the secondary coil R_S is calculated with respect to the electrical resistivity ρ_c of the conductor material, the dimensions of the implanted coil, and the construction and number of windings. For this, the bending of the conductor is taken into account, which leads to a lower resistance on the inner side of the conductor (lower diameter) compared to the outer side of the conductor (higher diameter).

The resistance of the short circuit connection R_{SC} from the first to the last winding of the coils is taken into account by assuming a thin copper foil underneath the wire windings (WWC) with a resistance of $R_{SC} = 500$ mΩ and by assuming two thin copper wires on each side of the coil with an overall resistance of $R_{SC} = 1$ mΩ (FWC). The dimensions of the short circuit connection are neglected when determining the diameter of the core, the diameter of the coil wire d_W, and the thickness of the layer d_L based on the maximum coil diameter d_{max} and the maximum coil length l_{max} (see Fig. 4). Additionally, for serial compensated secondary coils, an equivalent series resistance (ESR) of $R_{ESR} = 2$ mΩ is assumed for the compensating capacitors. For both types of secondary coils, the conductor resistance reveals to

$$R_S = R_{SC} + R_{ESR}$$
$$+ \begin{cases} -\dfrac{2 \cdot \rho_c \cdot N_S}{\sqrt{d_{max}^2 - d_W^2} - d_{max}} & \text{WWC} \\ \dfrac{2 \cdot \pi \cdot \rho_c}{l_{max}} \cdot \displaystyle\sum_{n=1}^{N_S} \dfrac{1}{\ln\left(\frac{d_{max}-(n-1)\cdot d_F}{d_{max}-n\cdot d_F}\right)} & \text{FWC.} \end{cases} \quad (17)$$

In Fig. 8, R_S for WWC and FWC with 10 windings is shown assuming an electrical resistivity $\rho_c = 17.25$ n$\Omega \cdot$ m for representing a copper conductor according to [45].

With increasing frequency of the alternating magnetic field, the resistance of the secondary coil is influenced by the skin effect. This is considered in the analytic model by determining the skin depth and adjusting the cross sectional area of the conductor accordingly in case the diameter of the wire (WWC) or the thickness of the layer (FWC) exceeds the skin depth. The influence of the proximity effect on the conductor resistance is neglected in this analysis.

B. HEATING POWER

The temperature of the implanted secondary coil is increased based on the heating power $P_{S,H}$. This is one of the key parameters for generating an appropriate rise of temperature in the surrounding tumor tissue and hence for conducting a successful ablation of the tumor. The heating power is converted into heat by the resistance R_S of the coil conductor.

With

$$\underline{S}_S = \frac{U_S \cdot \underline{I}_S^*}{2}, \quad (18)$$

the power $\underline{S}_S$ in the secondary coil reveals to (19), as shown at the bottom of the next page.

The power contributing to heat generation is determined with

$$P_{S,H} = \text{Re}\left(\underline{S}_S\right) \quad (20)$$

and maximized by choosing the appropriate compensating capacitor C_S for the serial reactive power compensation. With this, the heating power in the secondary coil reveals to

$$P_{S,H} = \begin{cases} \dfrac{R_S \cdot \omega^2 \cdot \left|\underline{\Psi}_{PS}\right|^2}{2 \cdot \left(R_S^2 + \omega^2 \cdot N_S^4 \cdot \Lambda_S^2\right)} & \text{UC} \\ \dfrac{\omega^2 \cdot \left|\underline{\Psi}_{PS}\right|^2}{2 \cdot R_S} & \text{SC.} \end{cases} \quad (21)$$

In case of an uncompensated secondary coil, the maximum possible heating power $P_{S,H,max}$ reveals to

$$P_{S,H,max} = \frac{\omega \cdot \left|\underline{\Psi}_{PS}\right|^2}{4 \cdot N_S^2 \cdot \Lambda_S} \quad (22)$$

for a conductor resistance

$$R_{S,max} = \omega \cdot N_S^2 \cdot \Lambda_S, \quad (23)$$

whereas the heating power $P_{S,H}$ increases with decreasing conductor resistance R_S for a serial compensated secondary coil according to (21). Hence, the electrical resistivity ρ_c of the coil conductor material has to be as low as possible and a coil design, which minimizes R_S and which maximizes $\left|\underline{\Psi}_{PS}\right|$, has to be chosen for achieving maximum heating power. $R_{S,max}$ for both secondary coil types resulting from a copper conductor is shown in Fig. 8.
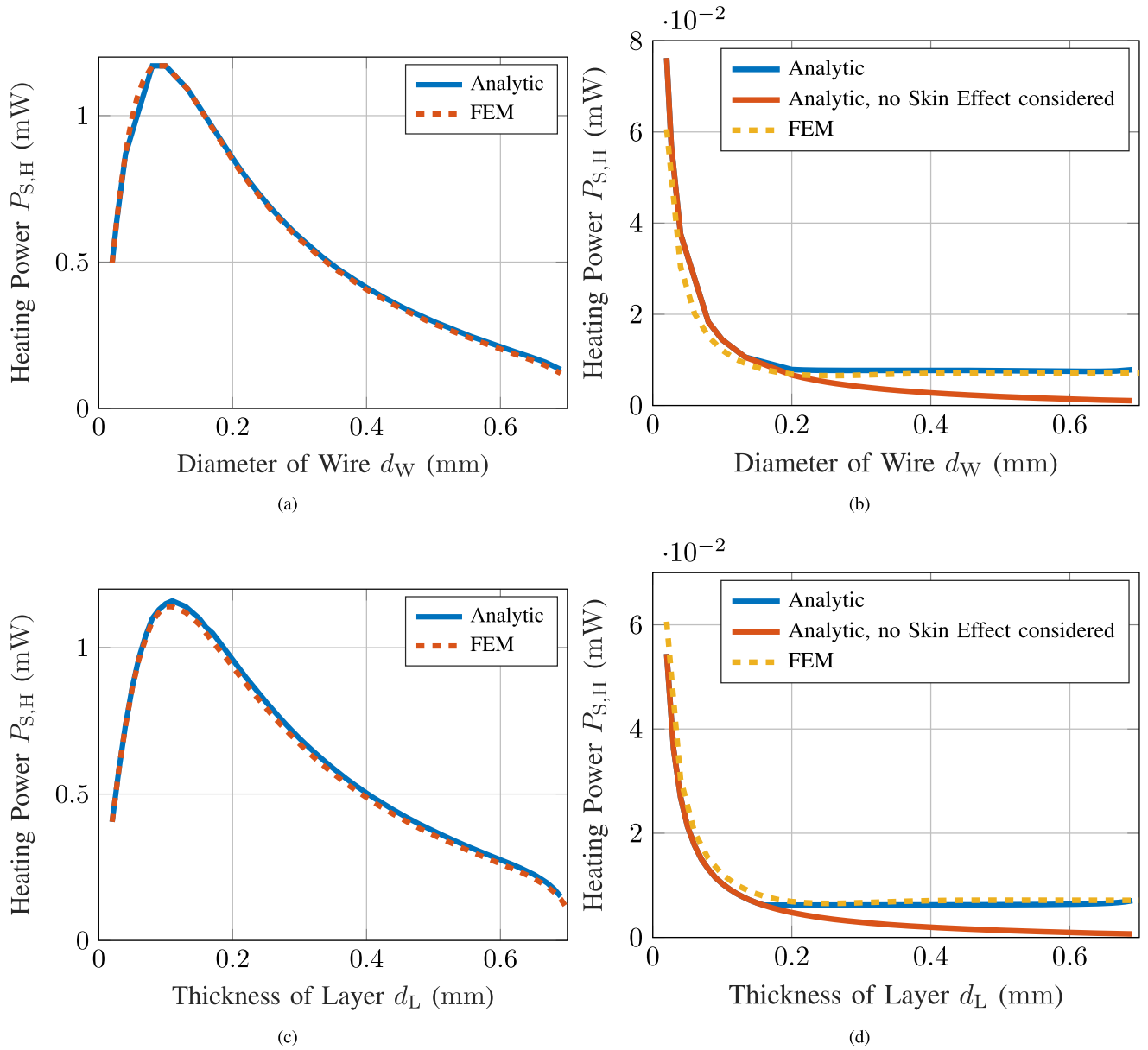
FIGURE 9. Comparison of the results of the analytic calculation of the heating power $P_{S,H}$ for an uncompensated WWC and an uncompensated FWC to the heating power evaluated by a FEM simulation for a magnitude of the primary magnetic field strength $H_P = 50\,\frac{A}{m}$, a frequency of the magnetic field $f = 100$ kHz, and a relative permeability of the coil core $\mu_r = 2100$. No short circuit connection resistances are taken into account for this comparison. (a) WWC with $\rho_c = 1.6\,\mu\Omega \cdot m$, (b) WWC with $\rho_c = 10\,n\Omega \cdot m$, (c) FWC with 10 windings and with $\rho_c = 2.8\,\mu\Omega \cdot m$, and (d) FWC with a single winding and with $\rho_c = 10\,n\Omega \cdot m$.

VI. RESULTS AND VALIDATION

To validate the combined numerical-analytic analysis, FEM simulations are carried out for specific parameter sets and the resulting heating power of both analyses are compared.

No short circuit connection resistances between the start and the end of the coil conductors are taken into account for the validation with FEM. In Fig. 9, the comparison for WWC and FWC with a low conductive conductor material is shown for

$$\underline{S}_S = \begin{cases} \dfrac{R_S \cdot \omega^2 \cdot \left|\underline{\Psi}_{PS}\right|^2}{2 \cdot \left(R_S^2 + \omega^2 \cdot N_S^4 \cdot \Lambda_S^2\right)} & \text{UC} \\[4mm] \dfrac{0.5 \cdot C_S \cdot \omega^3 \cdot \left|\underline{\Psi}_{PS}\right|^2 \cdot (\omega \cdot C_S \cdot R_S - \text{j})}{C_S^2 \cdot R_S^2 \cdot \omega^2 + C_S^2 \cdot \omega^4 \cdot N_S^4 \cdot \Lambda_S^2 - 2 \cdot \omega^2 \cdot C_S \cdot N_S^2 \cdot \Lambda_S + 1} & \text{SC.} \end{cases} \tag{19}$$
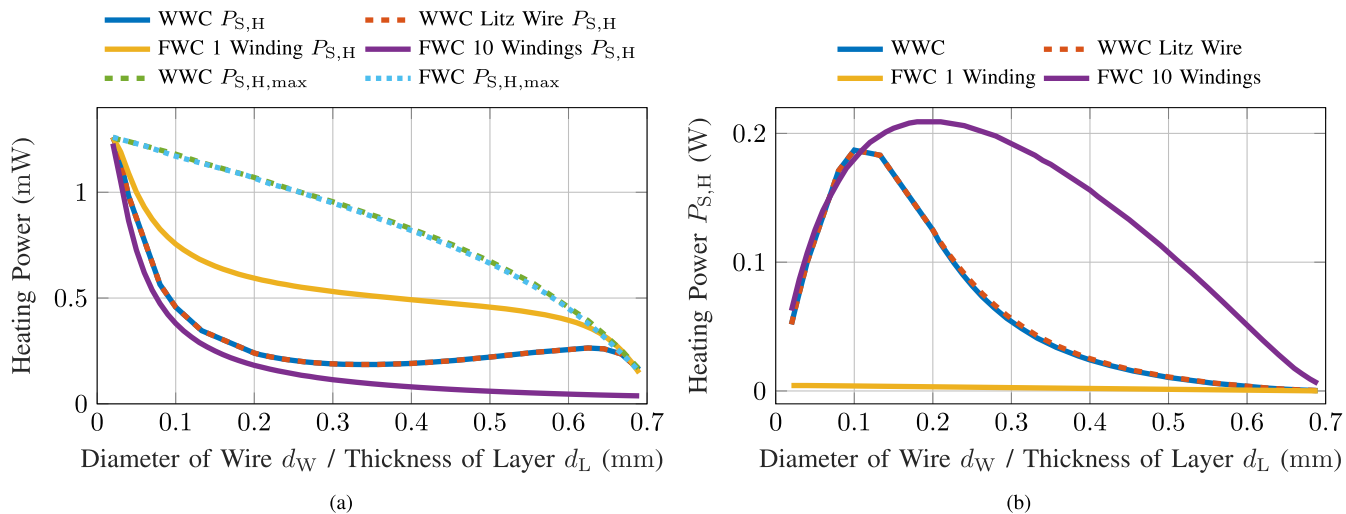
FIGURE 10. Heating power $P_{\mathrm{S,H}}$ and maximum achievable heating power $P_{\mathrm{S,H,max}}$ for WWC and FWC for a magnitude of the primary magnetic field strength $H_{\mathrm{P}} = 50\ \frac{\mathrm{A}}{\mathrm{m}}$, a frequency of the magnetic field $f = 100$ kHz, and a relative permeability of the coil core $\mu_{\mathrm{r}} = 2100$. $P_{\mathrm{S,H}}$ is evaluated for a solid wire and for an appropriate litz wire to prevent an increase of R_{S} due to skin effect (WWC) as well as for a single winding and 10 windings (FWC). (a) Uncompensated secondary coils with $\rho_{\mathrm{c}} = 325$ n$\Omega \cdot$ m (WWC) and with $\rho_{\mathrm{c}} = 375$ n$\Omega \cdot$ m (FWC), (b) serial compensated secondary coils with $\rho_{\mathrm{c}} = 16$ n$\Omega \cdot$ m.

TABLE 2. Optimized parameters for maximum heating power.

	WWC UC	FWC UC	WWC SC	FWC SC
Heating Power $P_{\mathrm{S,H}}$ for $H_{\mathrm{P}} = 50\ \frac{\mathrm{A}}{\mathrm{m}}$ (mW)	1.26	1.26	189	209
Heating Power $P_{\mathrm{S,H,1}}$ for $H_{\mathrm{P}} = 1\ \frac{\mathrm{A}}{\mathrm{m}}$ (μW)	0.503	0.503	75.6	83.7
Wire Diameter / Layer Thickness (mm)	0.02	0.02	0.11	0.20
Electrical Resistivity of Conductor (n$\Omega \cdot$ m)	325	375	16	16
Frequency (kHz)	100	100	100	100
Relative Permeability	2100	2100	2100	2100
Type of Wire (WWC) / Windings (FWC)	don't care	don't care	Litz Wire	10

one set of parameters. Additionally, the results for a very high conductive exemplary conductor material are compared for validating the consideration of the influence of the skin effect in the analytic model. For this, an electrical resistivity below the parameter set used in this paper is assumed for increasing the influence of the skin effect. The comparison shows a good correspondence of the numerical-analytic results to the results of the FEM simulation for the parameter sets applied in Fig. 9 as well as for further parameter sets with different frequency and different relative permeability of the core.

In addition to the validation by FEM simulations, a basic experimental prototype measurement is done. For this, a nearly homogeneous alternating magnetic field with $H_{\mathrm{P}} = 1840\ \frac{\mathrm{A}}{\mathrm{m}}$ and a frequency of 102 kHz is generated by two primary coils in a Helmholtz configuration. A single winding of copper foil with a thickness of 40 μm is applied to a cylindrical ferrite core with a diameter of approximately 1.45 mm, a length of 20 mm, and a relative permeability of approximately 2300 for representing an uncompensated

FWC with a single winding. With this, the heating power results in approximately 0.7 W, which corresponds to the heating power of 0.67 W resulting from the numerical-analytic calculations. However, for a conclusive experimental prototype measurement, a precise measurement setup has to be realized subsequent to this paper along with different types of implanted coils.

In case the resistance of the short circuit connection and the ESR is low compared to the resistance of the coil conductor and as long as the thickness of the conductive layer d_{L} remains constant and the skin effect can be neglected, the number of windings of FWC does not influence the resulting heating power. However, in case the short circuit resistance, the ESR, and the influence of the skin effect has to be taken into account, the maximum heating power increases with increasing number of windings due to $\frac{|\Psi_{\mathrm{PS}}|}{R_{\mathrm{S}}}$ is increased by reducing the thickness of each single winding, which decreases the influence of the skin effect, and by increasing $\frac{R_{\mathrm{S}}}{R_{\mathrm{SC}}+R_{\mathrm{ESR}}}$. As shown in Fig. 10, WWC and FWC reveal the same values for $P_{\mathrm{S,H}}$ and $P_{\mathrm{S,H,max}}$ with respect to the diameter of the coil wire and with respect to the thickness of the conductive layer for a different electrical resistivity of the conductor material. Hence, by choosing the appropriate coil type, $\underline{U}_{\mathrm{S}}$ and $\underline{I}_{\mathrm{S}}$ can be influenced without changing the heating power due to a different inductance L_{S} and a different linked magnetic flux $\underline{\Psi}_{\mathrm{PS}}$.

Within the parameter sets considered in this work, an optimization with respect to maximize the heating power is carried out. Regarding this optimization, maximum heating power is achieved for $d_{\mathrm{W}} = d_{\mathrm{L}} = 0.02$ mm, $\rho_{\mathrm{c}} = 325$ n$\Omega \cdot$ m (WWC), and $\rho_{\mathrm{c}} = 375$ n$\Omega \cdot$ m (FWC) in case no reactive power compensation is used, whereas, according to (21), the lowest value of ρ_{c} in the parameter
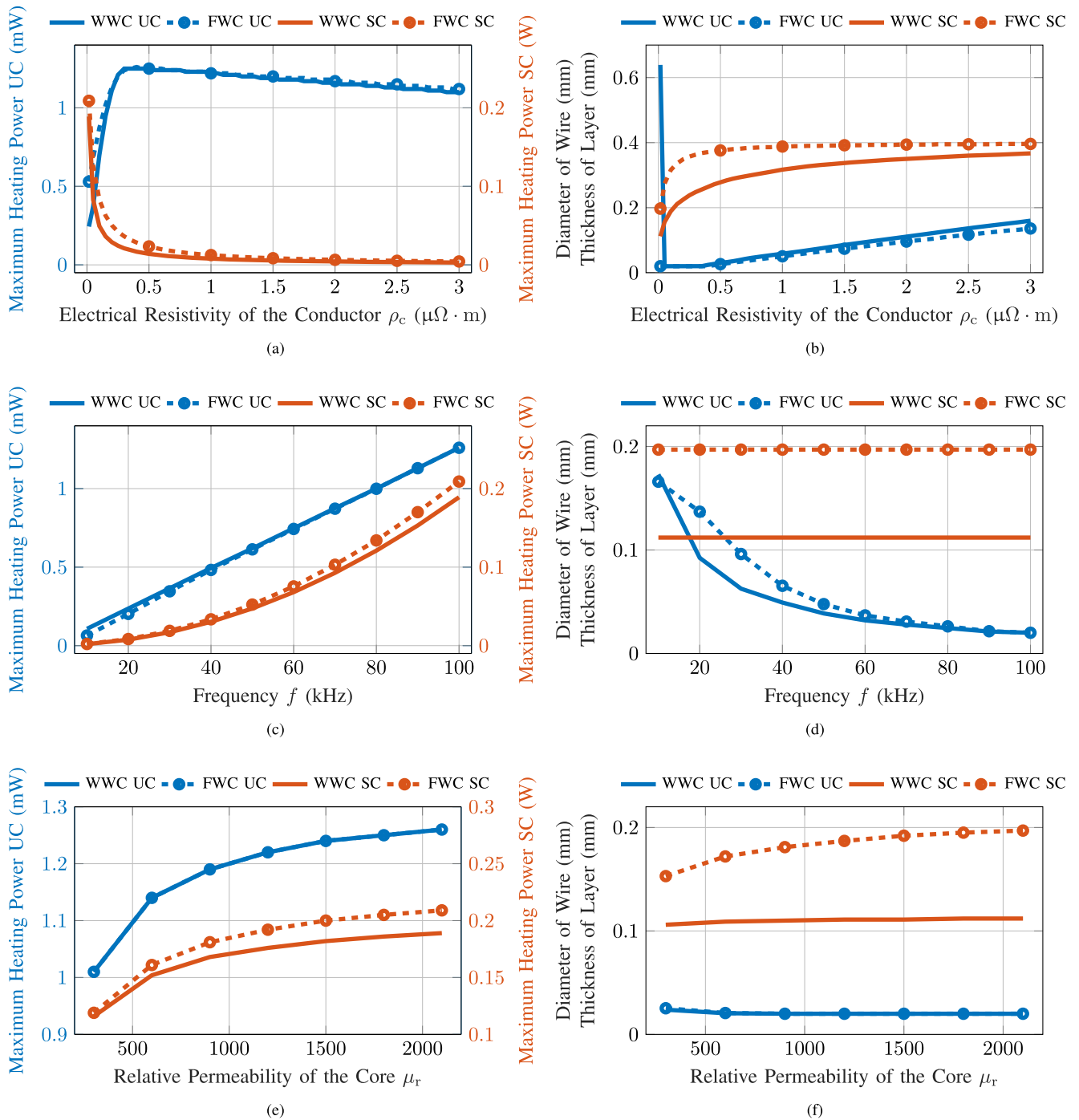
FIGURE 11. Dependency of the maximum heating power, the corresponding diameter of wire, and the corresponding thickness of layer, which reveal maximum heating power, on the parameter sets for $H_P = 50 \frac{A}{m}$ and for WWC UC with solid wire, FWC UC with a single winding, WWC SC with litz wire and FWC SC with 10 windings. (a), (b) Dependency on the electrical resistivity of the conductor material for $f = 100$ kHz and $\mu_r = 2100$, (c), (d) dependency on the frequency of the alternating primary magnetic field for $\rho_c = 325$ n$\Omega \cdot$ m (WWC UC), $\rho_c = 375$ n$\Omega \cdot$ m (FWC UC), $\rho_c = 16$ n$\Omega \cdot$ m (WWC SC, FWC SC), and $\mu_r = 2100$, (e), (f) dependency on the relative permeability of the core for $\rho_c = 325$ n$\Omega \cdot$ m (WWC UC), $\rho_c = 375$ n$\Omega \cdot$ m (FWC UC), $\rho_c = 16$ n$\Omega \cdot$ m (WWC SC, FWC SC), and $f = 100$ kHz.

set ($\rho_c = 16$ n$\Omega \cdot$ m) reveals maximum heating power for $d_W = 0.11$ mm (WWC with litz wire) and $d_L = 0.20$ mm (FWC with 10 windings) in case of a serial compensated secondary coil. With respect to the frequency of the alternating magnetic field and to the relative permeability of the core, the maximum values of these parameters in the parameter

sets ($f = 100$ kHz and $\mu_r = 2100$) reveal the maximum heating power. The results of this evaluation are presented in Fig. 10. In Table 2, a summary on the parameters for achieving maximum heating power is given. Considering all coil types, a maximum heating power of $P_{S,H} = 189$ mW is achieved by a serial compensated WWC, whereas a FWC

with 10 windings reveals $P_{S,H} = 209$ mW for the parameter set presented above and for a primary magnetic field strength of $H_P = 50 \frac{A}{m}$. For up to approximately 80 windings, the heating power of a serial compensated FWC increases to a maximum of $P_{S,H} \approx 1.3$ W at $d_L = 0.40$ mm. For more than 80 windings, the heating power does not increase further. However, the single layers of foil have to be extremely thin for the realization of such a high number of windings.

According to $|\underline{\Psi}_{PS}| \propto H_P$ and $P_{S,H} \propto |\underline{\Psi}_{PS}|^2$, the maximum heating power can be determined for any magnitude H_P of the primary alternating magnetic field for all coil types with

$$P_{S,H} = \left(\frac{H_P}{H_1}\right)^2 \cdot P_{S,H,1}, \qquad (24)$$

where $P_{S,H,1}$ denotes the resulting heating power for $H_P = H_1 = 1 \frac{A}{m}$. $P_{S,H,1}$ is presented in Table 2 for all coil types and for all types of reactive power compensation analyzed in this publication.

Fig. 11 presents the dependencies of the maximum heating power on the electrical resistivity of the conductor material, on the frequency of the alternating primary magnetic field, and on the relative permeability of the core along with the corresponding diameter of wire and the corresponding thickness of layer for achieving maximum heating power for $H_P = 50 \frac{A}{m}$. In case of an uncompensated secondary coil, a particular electrical resistivity exits for achieving maximum heating power. For an increasing ρ_c, the maximum heating power decreases and the diameter of wire (WWC) and the thickness of layer (FWC) increases. For decreasing ρ_c, the maximum heating power rapidly decreases, whereas d_W and d_L remain constant at 0.02 mm due to this is the lowest value in the parameter set analyzed in this work. In case of a WWC, d_W rapidly increases to 0.64 mm for a low electrical resistivity of the conductor material. For serial compensated secondary coils, the maximum heating power is achieved for the lowest electrical resistivity in the parameter set. d_W and d_L increase for increasing ρ_c and converge to $d_W = 0.42$ mm (WWC) and $d_L = 0.40$ mm (FWC) for high ρ_c. In case of increasing frequency, the maximum heating power for all coil types and compensation types increases as well, whereas the diameter of wire and the thickness of layer decrease for uncompensated secondary coils and remain constant at $d_W = 0.11$ mm (WWC) and at $d_L = 0.20$ mm (FWC) for secondary coils with serial reactive power compensation. The maximum heating power increases with increasing relative permeability of the core for uncompensated secondary coils and converges to $P_{S,H} \approx 1.3$ mW (WWC and FWC) for very high values of μ_r. For serial compensated secondary coils, the heating power increases as well with increasing μ_r and converges to $P_{S,H} \approx 220$ mW (WWC) and $P_{S,H} \approx 240$ mW (FWC) for very high values of μ_r. The diameter of wire and the thickness of layer slightly decrease to and remain constant at 0.02 mm for $\mu_r > 300$ in case of an uncompensated secondary coil, whereas, for secondary coils with serial reactive power compensation, d_W slightly increases and converges to

TABLE 3. Material properties used in the thermal evaluation.

Material Property	Tumor $\leq 50°$C	Tumor $\geq 100°$C	Core	Conductor Material
Thermal Conductivity (W/(m · K))	0.54	0.33	4.3	401
Specific Heat Capacity (J/(kg · K))	3772	2309	800	384
Density (kg/m³)	1072	1072	4800	8960

0.12 mm (WWC) and d_L increases and converges to 0.22 mm (FWC) for very high values of μ_r.

VII. PERFORMANCE

With respect to tumor treatment, the heat generated by an implanted secondary coil with a specific heating power and the resulting rise of temperature in the surrounding tissue has to be known. Additionally, unwanted tissue heating outside of the tumor by eddy currents has to be taken into account for ensuring the safety of the patients. In this section, a thermal evaluation is performed and the resulting SAR is evaluated. Furthermore, the PTE and the coupling coefficient with respect to two configurations of primary coils are determined and the impact of an angular or lateral misalignment of the secondary coil as well as the impact of body tissue on heating power and on coil design are discussed.

A. THERMAL EVALUATION

For determining the minimum heating power, which is required to heat human tissue above the necrosis temperature of 50°C [14], [46] for being able to conduct a thermal tumor ablation, a thermal evaluation is carried out. Based on this minimum heating power, the minimum magnitude of the primary magnetic field strength is determined for all coil types and all compensation types with respect to the optimized parameter set, which reveals maximum heating power.

The thermal evaluation is done by a FEM simulation. A spherical area of human tissue with a diameter of 200 mm is used in the model. The cylindrical secondary coil is represented by a cylinder surrounded by a heat generating layer with a total diameter of d_{max} and is placed in the center of the sphere. The thermal properties of copper [45] are assigned to the surrounding layer which are assumed to be similar to the thermal properties of a conductor material with a different electrical resistivity. Furthermore, the typical thermal properties of a ferrite material [47] are assigned to the core. As done in [48], the thermal properties of the tumor are defined to be similar to the surrounding tissue. A kidney tumor is assumed due to this represents a challenging scenario with respect to tissue heating based on the combination of a high specific heat capacity, a high thermal conductivity and a high density. All thermal tissue properties are taken from [49]. The thermal conductivity and the heat capacity of tissue depend on water content [50]–[52]. Hence, based on the desiccation of tissue with rising tissue temperature [53], the thermal conductivity and the heat capacity decrease with increasing temperature. Therefore, these thermal properties are reduced linearly between 50°C and 100°C. The resulting
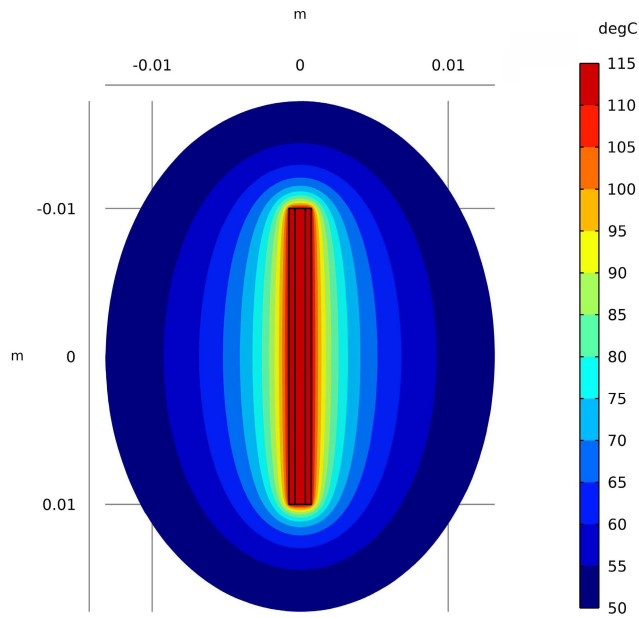
FIGURE 12. Temperature in the cross section of the model of the secondary coil used in the thermal evaluation including the surrounding tissue for a heating power of $P_{S,H} = 1.5$ W. Solely tissue with a temperature of and above the necrosis temperature of 50°C is shown. A maximum tissue temperature of 114°C is achieved.

TABLE 4. Performance evaluation for optimized implanted coils.

	WWC UC	FWC UC	WWC SC	FWC SC
Heating Power, PDL (W)	1.5			
Maximum Tissue Temperature (°C)	114			
Width of Spheroidal Ablation Area (mm)	27.5			
Length of Spheroidal Ablation Area (mm)	34			
Primary Magnetic Field Strength H_P (A/m)	1727	1727	141	134
SAR Single Longitudinal Coil (mW/kg)	306	306	2.04	1.84
SAR Optimized Helmholtz Coil (mW/kg)	887	887	5.91	5.34
PTE Single Longitudinal Coil ($\cdot 10^{-3}$)	4.62	4.62	411	436
PTE Optimized Helmholtz Coil ($\cdot 10^{-3}$)	0.97	0.97	128	139
k Single Longitudinal Coil ($\cdot 10^{-3}$)	2.49	2.49	2.40	2.30
k Optimized Helmholtz Coil ($\cdot 10^{-3}$)	1.10	1.10	1.05	1.01

thermal material properties are summarized in Table 3. On the outside boundaries of the spherical area of human tissue, a constant temperature of 37°C is defined to represent the thermal interface to the surrounding part of the human body, which keeps the boundaries at body temperature. However, as the surrounding part of the body is heated as well in real-life thermal tumor ablations, this is a worst case scenario with respect to increasing tissue temperature for simplifying the thermal FEM model.

As shown in Fig. 12, a heating power of $P_{S,H} = 1.5$ W reveals a tissue temperature above the necrosis temperature in a distance up to 7 mm in the axial direction and in a distance up to 13 mm in radial direction to the cylindrical secondary coil. Thus, a spheroidal tumor with 34 mm in length and 27.5 mm in width can be ablated. Furthermore, a maximum tissue temperature of 114°C is achieved by a heating power of 1.5 W. The resulting required magnitude of the primary magnetic field strength for all optimized coil

types and compensation types is presented in Table 4 along with a summary of the results of the thermal evaluation.

B. SPECIFIC ABSORPTION RATE

With respect to unwanted heating of healthy tissue, the SAR is the key parameter for the evaluation of the influence of eddy currents on tissue temperature. The SAR is defined as

$$\text{SAR} = \frac{J^2}{2 \cdot \rho_{\text{dens,B}} \cdot \sigma_B}, \qquad (25)$$

where J denotes the magnitude of the local current density within the body tissue, $\rho_{\text{dens,B}}$ denotes the density, and σ_B denotes the electrical conductivity of the body tissue. In [42], different primary coil configurations are analyzed and compared and the resulting SAR for each coil configuration is evaluated at a frequency of $f = 100$ kHz based on a model of the human body with respect to unwanted tissue heating. In case the frequency of the primary alternating magnetic field, the electrical conductivity, and the density of the body tissue remain constant, the resulting SAR can be calculated for each primary coil system with

$$\text{SAR} = \left(\frac{H_P}{H_{\text{ref}}}\right)^2 \cdot \text{SAR}_{\text{ref}} \qquad (26)$$

based on the magnetic field strength H_P needed for generating the required heating power evaluated in Section VII-A ($P_{S,H} = 1.5$ W), which is necessary for achieving an adequate rise of tissue temperature.

In (26), H_{ref} and SAR_{ref} can be taken from [42] (Table VIII, column $H_{\text{TA,av}}$ and column SAR). The resulting SAR for a single longitudinal primary coil (SiCLoC) and an optimized Helmholtz primary coil (DCHC) is presented in Table 4. For these coil types, the SAR remains below the limit defined in [54] (2 $\frac{\text{W}}{\text{kg}}$) for uncompensated as well as for serial compensated secondary coils. This limit is considered to not cause a rise of tissue temperature and therefore to not cause physiological stress for patients.

C. POWER TRANSFER EFFICIENCY AND COUPLING COEFFICIENT

As done in Section VII-B, the PTE and the coupling coefficient between the primary coils and the implanted secondary coil is evaluated based on the primary coil configurations analyzed in [42]. For determining the PTE, 10 windings are assumed for each single coil of the primary coil configurations. The results are presented in Fig. 13. The coupling coefficient shows a negligible dependency on the type of secondary coil and on the number of windings of FWC. The maximum PTE is achieved for the same diameter of wire d_W and for the same thickness of layer d_L on which the heating power is at maximum, due to a low coupling between the primary coils and the secondary coil and therefore a primary current with constant magnitude is assumed. The low coupling is confirmed by the evaluation of the coupling coefficient k in Fig. 13c, which reveals a maximum of
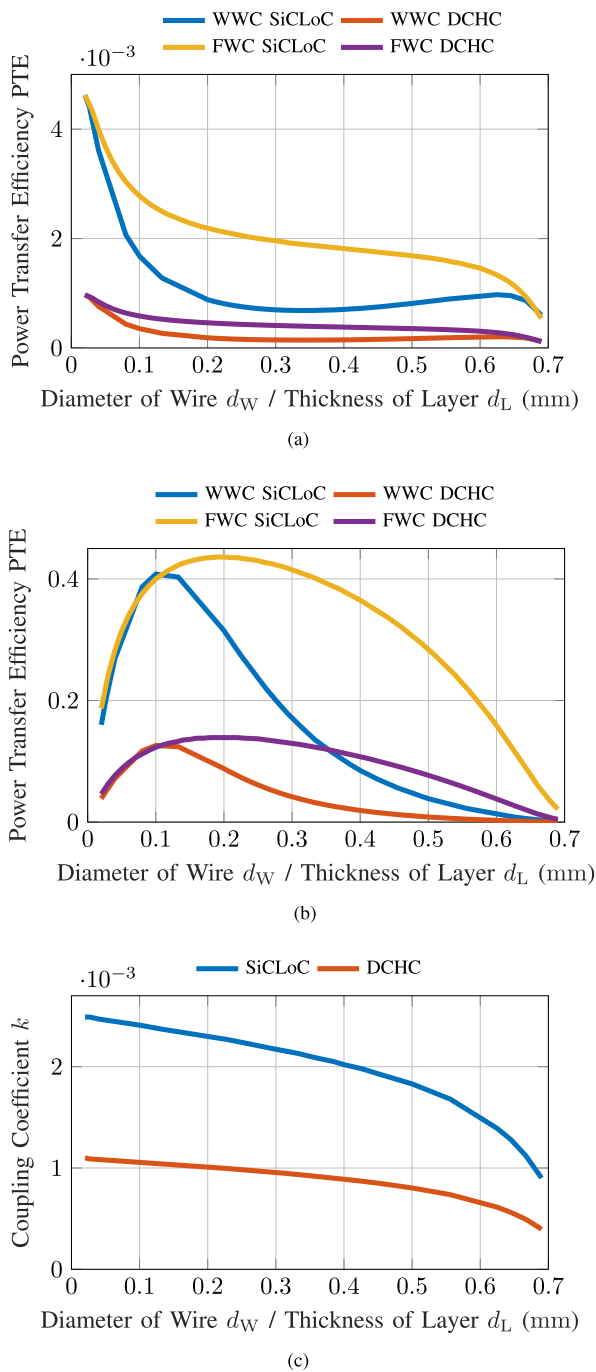
FIGURE 13. Power transfer efficiency and coupling coefficient with respect to a single longitudinal primary coil (SiCLoC) and to an optimized Helmholtz primary coil (DCHC) as defined in [42] for $f = 100$ kHz and $\mu_r = 2100$. The PTE is evaluated assuming 10 windings for each single coil of the primary coil configurations. (a) Uncompensated WWC and FWC with a single winding for $\rho_c = 325$ n$\Omega \cdot$ m (WWC) and for $\rho_c = 375$ n$\Omega \cdot$ m (FWC), (b) serial compensated WWC and FWC with 10 windings for $\rho_c = 16$ n$\Omega \cdot$ m, (c) coupling coefficient k. The results for k show a negligible dependency on secondary coil type and on the number of FWC windings.

$k = 2.49 \cdot 10^{-3}$ (SiCLoC) and of $k = 1.1 \cdot 10^{-3}$ (DCHC) for $d_W = d_L = 0.02$ mm. PTE and k for all optimized secondary coil types are summarized in Table 4. For secondary coil types with serial reactive power compensation, the maximum PTE

and the maximum coupling coefficient are not achieved at the same diameter of wire or the same thickness of layer, respectively.

D. MISALIGNMENT

In the analysis done in this publication, the field lines of the homogeneous primary magnetic field are assumed to be parallel to the axis of the core of the secondary coil. In case of an angular misalignment of the secondary coil with respect to the field lines of the primary magnetic field, the magnitude $H_{||}$ of the primary magnetic field component, which is parallel to the axis of the coil, can be approximated with

$$H_{||} \approx H_P \cdot \cos(\alpha), \tag{27}$$

where α denotes the angle between the field lines and the axis of the coil core. As a coil core with $\mu_r > 1$ influences the spatial distribution of the primary magnetic field, a field component, which is parallel to the core of the coil, exists even for $\alpha = 90°$. This parallel field component can be neglected for the dimensions of the secondary coil assumed in this paper.

The impact of a lateral misalignment depends on the spatial distribution of the primary magnetic field and hence depends on the specific primary coil configuration. For all coil configurations analyzed in [42], a nearly homogeneous magnetic field is generated within a spherical area with a diameter of 40 mm surrounding the implanted coil. Therefore, the impact of a lateral misalignment on the heating performance can be neglected within this area for all primary coil configurations presented in [42].

E. IMPACT OF BODY TISSUE

In contrast to the thermal evaluation in Section VII-A, the impact of the tissue surrounding the implanted coils is not taken into account by the numerical-analytic calculation of the heating power as the influence of the body tissue on the heating power, the coil properties, and the coil design has shown to be negligible. This is due to the maximum electrical conductivity and the relative permeability of human tissue are negligibly low compared to the electrical conductivity of the conductor material and the relative permeability of the coil core. Additionally, within the frequency range considered in the present paper, the impact of the patient's body tissue on the alternating primary magnetic field caused by eddy currents induced in the body tissue turned out to be negligibly low as well.

VIII. DISCUSSION

The results of the numerical-analytic analysis done in this paper shows the possibility to significantly enhance the performance of a contactless thermal tumor ablation by choosing an appropriate design of the heat generating implanted coil. In most cases, FWC yields more heating power compared to WWC based on the same diameter of wire or thickness of layer, respectively. However, by choosing a conductor material with an appropriate electrical resistivity, the same

heating power can be achieved with uncompensated WWC and FWC, as shown by $P_{S,H,max}$ in Fig. 10, whereas a serial compensated FWC provides more heating power than a WWC with serial reactive power compensation. Regarding the mechanical construction of the implanted coils, WWC requires more construction effort compared to FWC due to the number of windings is much higher. Additionally, the short circuit connection needs to be longer and causes a slight deformation of the single windings, which has not been taken into account in this analysis.

The heating power of different types of ferromagnetic implants have been analyzed and optimized in the last decades. A maximum heating power per implant length in the range from approximately $18 \frac{W}{m}$ to $40 \frac{W}{m}$ have been reported by the authors in [39] and [40] for heat generation by eddy currents within the implant and approximately $47 \frac{W}{m}$ have been achieved by adding a metallic sheath surrounding a ferrite core in [41]. An uncompensated optimized implanted secondary coil proposed in this paper shows less maximum heating power per implant length (approximately $37 \frac{W}{m}$) compared the results shown in [39] (approximately $40 \frac{W}{m}$) for equal conditions ($H_P = 1.5 \frac{kA}{m}$ peak, $f = 100$ kHz, $\mu_r = 150$). Moreover, the implant diameter in [39] is 0.1 mm less (1.4 mm) than the implant diameter used in the present publication. In contrast to this, an uncompensated optimized implanted secondary coil (FWC) reveals about 2.4 times more heating power per unit length ($113 \frac{W}{m}$) compared to the results reported in [41] ($47 \frac{W}{m}$) for a ferrite core surrounded by a metallic sheath with an overall diameter of 1.5 mm and a length of 24.85 mm ($H_P \approx 1.5 \frac{kA}{m}$ rms, $f \approx 100$ kHz, $\mu_r \approx 2000$ at 50°C).

IX. CONCLUSION

With the numerical-analytic analysis carried out in the present publication, a way for precisely and efficiently evaluating the heating power of implanted wire wound and foil wound coils with restricted dimensions for a thermal tumor ablation of deep-seated tumors is presented. Based on the results of this paper, the optimum design of the implanted coil can be determined with respect to different limiting conditions, such as a specific diameter of the conductor or a specific operating frequency. However, the thermal model is kept simple and the influence of blood flow is not taken into account in the thermal analysis. Moreover, the resistance of the short circuit connection of the coils and the ESR of the compensating capacitor are solely considered to some extent with constant values and hot spot generation on these resistances is not taken into account in the thermal analysis. Additionally, the spatial requirements and the inductance of the short circuit connection and the compensating capacitors are assumed to be negligibly small. Subsequent to this paper, a precise experimental measurement setup has to be realized for an additional validation of the results achieved in this work.

The SAR is kept well below the limits published in international standards with uncompensated and serial compensated implanted coils. Hence, an appropriate rise of temperature within the tumor can be achieved while preventing to cause physiological stress for patients by heating healthy tissue. Generally, by maximizing the ratio of heating power to required primary magnetic field strength, the risk of unwanted heating and influencing of other implanted devices, such as pacemakers, artificial joints, screws, plates, clips, and stents, is minimized, which enhances the safety and the well-being of the patients as well as the outcome of the tumor treatment.

REFERENCES

[1] J. Heinrich and N. Parspour, "Contribution to the development of positioning tolerant inductive charging systems," in *Proc. Emobility-Electr. Power Train*, Nov. 2010, pp. 1–5.

[2] G. A. Covic and J. T. Boys, "Inductive power transfer," *Proc. IEEE*, vol. 101, no. 6, pp. 1276–1289, Jun. 2013.

[3] F. Musavi and W. Eberle, "Overview of wireless power transfer technologies for electric vehicle battery charging," *IET Power Electron.*, vol. 7, no. 1, pp. 60–66, Jan. 2014.

[4] S. Li and C. C. Mi, "Wireless power transfer for electric vehicle applications," *IEEE J. Emerg. Sel. Topics Power Electron.*, vol. 3, no. 1, pp. 4–17, Mar. 2015.

[5] M. Maier, D. Maier, M. Zimmer, and N. Parspour, "A novel self oscillating power electronics for contactless energy transfer and frequency shift keying modulation," in *Proc. Int. Symp. Power Electron., Electr. Drives, Autom. Motion (SPEEDAM)*, Jun. 2016, pp. 67–72.

[6] A. Zaheer, M. Neath, H. Z. Z. Beh, and G. A. Covic, "A dynamic EV charging system for slow moving traffic applications," *IEEE Trans. Transp. Electrific.*, vol. 3, no. 2, pp. 354–369, Jun. 2017.

[7] N. Parspour, D. Maier, and M. Böttigheimer, "Contactless energy transfer for charging electric and hybrid electric vehicles," in *Proc. 30th Int. Electr. Vehicle Symp. (EVS)*, vol. 5, 2017, pp. 3154–3162.

[8] M. Maier and N. Parspour, "Operation of an electrical excited synchronous machine by contactless energy transfer to the rotor," *IEEE Trans. Ind. Appl.*, vol. 54, no. 4, pp. 3217–3225, Jul. 2018.

[9] D. Niculae, M. Iordache, M. Stanculescu, M. L. Bobaru, and S. Deleanu, "A review of electric vehicles charging technologies stationary and dynamic," in *Proc. 11th Int. Symp. Adv. Topics Electr. Eng. (ATEE)*, Mar. 2019, pp. 1–4.

[10] T. Sun, X. Xie, and Z. Wang, "Design challenges of the wireless power transfer for medical microsystems," in *Proc. IEEE Int. Wireless Symp. (IWS)*, Apr. 2013, pp. 1–4.

[11] J. Walk, J. Weber, C. Soell, R. Weigel, G. Fischer, and T. Ussmueller, "Remote powered medical implants for telemonitoring," *Proc. IEEE*, vol. 102, no. 11, pp. 1811–1832, Nov. 2014.

[12] G. Xu, X. Yang, Q. Yang, J. Zhao, and Y. Li, "Design on magnetic coupling resonance wireless energy transmission and monitoring system for implanted devices," *IEEE Trans. Appl. Supercond.*, vol. 26, no. 4, pp. 1–4, Jun. 2016.

[13] P. R. Stauffer, C. J. Diederich, and M. H. Seegenschmiedt, "Interstitial heating technologies," in *Thermoradiotherapy and Thermochemotherapy*. Berlin, Germany: Springer, 1995, pp. 279–320.

[14] R. W. Y. Habash, R. Bansal, D. Krewski, and H. T. Alhafid, "Thermal therapy, Part 1: An introduction to thermal therapy," *Crit. Rev. Biomed. Eng.*, vol. 34, no. 6, pp. 459–489, 2006.

[15] R. W. Y. Habash, R. Bansal, D. Krewski, and H. T. Alhafid, "Thermal therapy, Part 2: Hyperthermia techniques," *Crit. Rev. Biomed. Eng.*, vol. 34, no. 6, pp. 491–542, 2006.

[16] H. Webb, M. G. Lubner, and J. L. Hinshaw, "Thermal ablation," *Seminars Roentgenol.*, vol. 46, no. 2, pp. 133–141, Apr. 2011.

[17] S. C. Tang, N. J. McDannold, and M. Vaninetti, "A wireless batteryless implantable radiofrequency lesioning device powered by intermediate-range segmented coil transmitter," in *Proc. 39th Annu. Int. Conf. IEEE Eng. Med. Biol. Soc. (EMBC)*, Jul. 2017, pp. 1966–1969.

[18] R. K. Gilchrist, R. Medal, W. D. Shorey, R. C. Hanselman, J. C. Parrott, and C. B. Taylor, "Selective inductive heating of lymph nodes," *Ann. Surg.*, vol. 146, no. 4, pp. 596–606, 1957.

[19] P. Moroz, S. K. Jones, and B. N. Gray, "Magnetically mediated hyperthermia: Current status and future directions," *Int. J. Hyperthermia*, vol. 18, no. 4, pp. 267–284, Jan. 2002.

[20] W. J. Atkinson, I. A. Brezovich, and D. P. Chakraborty, "Usable frequencies in hyperthermia with thermal seeds," *IEEE Trans. Biomed. Eng.*, vol. BME-31, no. 1, pp. 70–75, Jan. 1984.

[21] A. Y. Matloubieh, R. B. Roemer, and T. C. Cetas, "Numerical simulation of magnetic induction heating of tumors with ferromagnetic seed implants," *IEEE Trans. Biomed. Eng.*, vol. BME-31, no. 2, pp. 227–234, Feb. 1984.

[22] P. R. Stauffer, T. C. Cetas, A. M. Fletcher, D. W. Deyoung, M. W. Dewhirst, J. R. Oleson, and R. B. Roemer, "Observations on the use of ferromagnetic implants for inducing hyperthermia," *IEEE Trans. Biomed. Eng.*, vol. BME-31, no. 1, pp. 76–90, Jan. 1984.

[23] P. R. Stauffer, T. C. Cetas, and R. C. Jones, "Magnetic induction heating of ferromagnetic implants for inducing localized hyperthermia in deep-seated tumors," *IEEE Trans. Biomed. Eng.*, vol. BME-31, no. 2, pp. 235–251, Feb. 1984.

[24] J. A. Paulus, J. S. Richardson, R. D. Tucker, and J. B. Park, "Evaluation of inductively heated ferromagnetic alloy implants for therapeutic interstitial hyperthermia," *IEEE Trans. Biomed. Eng.*, vol. 43, no. 4, pp. 406–413, Apr. 1996.

[25] Y. Kotsuka and H. Okada, "Development of small and high efficiency implant for deep local hyperthermia," *Thermal Med. (Jpn. J. Hyperthermic Oncol.)*, vol. 19, no. 1, pp. 11–22, 2003.

[26] A. H. El-Sayed, A. A. Aly, N. I. Ei-Sayed, M. M. Mekawy, and A. A. Ei-Gendy, "Calculation of heating power generated from ferromagnetic thermal seed (PdCo-PdNi-CuNi) alloys used as interstitial hyperthermia implants," *J. Mater. Sci., Mater. Med.*, vol. 18, no. 3, pp. 523–528, Mar. 2007.

[27] C.-F. Huang, H.-Y. Chao, H.-H. Chang, and X.-Z. Lin, "A magnetic induction heating system with multi-cascaded coils and adjustable magnetic circuit for hyperthermia," *Electromagn. Biol. Med.*, vol. 35, no. 1, pp. 59–64, Jan. 2016.

[28] Z. Yang, W. Liu, and E. Basham, "Inductor modeling in wireless links for implantable electronics," *IEEE Trans. Magn.*, vol. 43, no. 10, pp. 3851–3860, Oct. 2007.

[29] A. K. Ram Rakhyani, S. Mirabbasi, and M. Chiao, "Design and optimization of resonance-based efficient wireless power delivery systems for biomedical implants," *IEEE Trans. Biomed. Circuits Syst.*, vol. 5, no. 1, pp. 48–63, Feb. 2011.

[30] B. Curran, U. Maaß, G. Fotheringham, N. Stevens, I. Ndip, and K.-D. Lang, "Modeling and characterization of PCB coils for inductive wireless charging," *Wireless Power Transf.*, vol. 2, no. 2, pp. 127–133, Sep. 2015.

[31] S. R. Khan and G. Choi, "Analysis and optimization of four-coil planar magnetically coupled printed spiral resonators," *Sensors*, vol. 16, no. 8, p. 1219, Aug. 2016.

[32] P. Feng, T. G. Constandinou, P. Yeon, and M. Ghovanloo, "Millimeter-scale integrated and wirewound coils for powering implantable neural microsystems," in *Proc. IEEE Biomed. Circuits Syst. Conf. (BioCAS)*, Oct. 2017.

[33] S. R. Khan, S. K. Pavuluri, and M. P. Y. Desmulliez, "Accurate modeling of coil inductance for near-field wireless power transfer," *IEEE Trans. Microw. Theory Techn.*, vol. 66, no. 9, pp. 4158–4169, Sep. 2018.

[34] H.-D. Lang and C. D. Sarris, "Optimal design of implants for magnetically mediated hyperthermia: A wireless power transfer approach," *J. Appl. Phys.*, vol. 122, no. 12, Sep. 2017, Art. no. 124701.

[35] G. Chen, C. Wang, Y. Cheng, and G. Wang, "Using metallic coil to optimize the heating efficiency for tumor hyperthermia," in *Proc. IEEE Wireless Power Transf. Conf. (WPTC)*, Jun. 2019.

[36] N. Soltani, M. ElAnsary, J. Xu, J. S. Filho, and R. Genov, "Safety-optimized inductive powering of implantable medical devices: Tutorial and comprehensive design guide," *IEEE Trans. Biomed. Circuits Syst.*, vol. 15, no. 6, pp. 1354–1367, Dec. 2021.

[37] Y. Cheng, G. Wang, and M. Ghovanloo, "Analytical modeling and optimization of small solenoid coils for millimeter-sized biomedical implants," *IEEE Trans. Microw. Theory Techn.*, vol. 65, no. 3, pp. 1024–1035, Mar. 2017.

[38] J. R. Wait, "Ferromagnetic implants in hyperthermia," *IEEE Trans. Biomed. Eng.*, vol. BME-32, no. 9, pp. 707–708, Sep. 1985.

[39] S. A. Haider, T. C. Cetas, J. R. Wait, and J.-S. Chen, "Power absorption in ferromagnetic implants from radiofrequency magnetic fields and the problem of optimization," *IEEE Trans. Microw. Theory Techn.*, vol. 39, no. 11, pp. 1817–1827, Nov. 1991.

[40] N. V. Wieringen, J. D. P. V. Dijk, G. J. Nieuwenhuys, C. E. Snel, and T. C. Cetas, "Power absorption and temperature control of multi-filament palladium–nickel thermoseeds for interstitial hyperthermia," *Phys. Med. Biol.*, vol. 41, no. 11, pp. 2367–2380, Nov. 1996.

[41] T. C. Cetas, E. J. Gross, and Y. Contractor, "A ferrite core/metallic sheath thermoseed for interstitial thermal therapies," *IEEE Trans. Biomed. Eng.*, vol. 45, no. 1, pp. 68–77, Jan. 1998.

[42] M. Prantner, N. Parspour, S. P. Haen, M. Böckeler, and J. Hetzel, "Analysis of coil configurations for a contactless thermal tumor ablation with implanted devices," *IEEE Trans. Biomed. Circuits Syst.*, vol. 16, no. 1, pp. 79–93, Feb. 2022.

[43] J. D. Jackson, *Klassische Elektrodynamik*. Berlin, Germany: Walter de Gruyter 2013.

[44] M. Albach, *Induktivitäten in der Leistungselektronik*. Wiesbaden, Germany: Springer Fachmedien Wiesbaden, 2017.

[45] D. R. Lide, *CRC Handbook of Chemistry and Physics*, 85th ed. Boca Raton, FL, USA: CRC Press, 2004.

[46] D. Haemmerich and P. F. Laeseke, "Thermal tumour ablation: Devices, clinical applications and future directions," *Int. J. Hyperthermia*, vol. 21, no. 8, pp. 755–760, Dec. 2005.

[47] *Ferrite Cores*, Magnetics, Division of Spang & Datasheet, Pittsburgh, PA, USA, 2021.

[48] S. M. Yacoob and N. S. Hassan, "FDTD analysis of a noninvasive hyperthermia system for brain tumors," *Biomed. Eng. OnLine*, vol. 11, no. 1, p. 47, 2012.

[49] R. L. Mcintosh and V. Anderson, "A comprehensive tissue properties database provided for the thermal assessment of a human at rest," *Biophysical Rev. Lett.*, vol. 5, no. 3, pp. 129–151, Sep. 2010.

[50] M. W. Chastagner, R. E. Dodde, A. J. Shih, W. Li, and R. K. Chen, "Measurement and modeling of tissue thermal conductivity with variable water content and compression," *J. Heat Transf.*, vol. 138, no. 7, Apr. 2016.

[51] M. Lipkin and J. D. Hardy, "Measurement of some thermal properties of human tissues," *J. Appl. Physiol.*, vol. 7, no. 2, pp. 212–217, Sep. 1954.

[52] K. Giering, I. Lamprecht, and O. Minet, "Specific heat capacities of human and animal tissues," *Proc. SPIE*, vol. 2624, pp. 188–197, Jan. 1996.

[53] D. Yang, M. C. Converse, D. M. Mahvi, and J. G. Webster, "Measurement and analysis of tissue temperature during microwave liver ablation," *IEEE Trans. Biomed. Eng.*, vol. 54, no. 1, pp. 150–155, Jan. 2007.

[54] *Medical Electrical Equipment—Part 2–33: Particular Requirements for the Basic Safety and Essential Performance of Magnetic Resonance Equipment for Medical Diagnosis*, International Electrotechnical Commission, Geneva, Switzerland, Standard IEC 60601-2-33:2010+AMD1:2013+AMD2:2015, 2015.

MICHAEL PRANTNER received the Dipl.-Ing. degree in electrical engineering from the University of Applied Sciences of Reutlingen, Reutlingen, Germany, in 2006.

He collected ten years of industrial experience, as a Hardware Design Engineer for biomedical systems in the field of electrosurgery with focus on power electronics at BOWA-electronic GmbH & Co. KG, Gomaringen, Germany, where he is currently the Head of the Research Group. His main research interest includes contactless energy transfer to devices inside the human body with focus on inductive systems.

NEJILA PARSPOUR received the master's degree in electrical engineering and the Ph.D. degree *(summa cum laude)* from the Technical University of Berlin, Berlin, Germany, in 1991 and 1995, respectively.

She collected five years of industrial experience with Philips and six years of scientific experience with the University of Bremen, Bremen, Germany. She is currently a Professor in electrical energy conversion with the University of Stuttgart, Stuttgart, Germany, and the Head of the Institute of Electrical Energy Conversion. Her research interests and teaching activities include electrical machines and drives with a focus on machine design and contactless energy transfer with a focus on inductive charging systems.

• • •